Collective Damage Growth Controls Fault Orientation in Quasibrittle Compressive Failure

Véronique Dansereau,[1] Vincent Démery,[2,3] Estelle Berthier,[4,5] Jérôme Weiss,[6] and Laurent Ponson[4]
[1]*Nansen Environmental and Remote Sensing Center, N-5006 Bergen, Norway*
[2]*Gulliver, CNRS, ESPCI Paris, PSL Research University, 10 rue Vauquelin, 75005 Paris, France*
[3]*Univ Lyon, ENS de Lyon, Univ Claude Bernard Lyon 1, CNRS, Laboratoire de Physique, F-69342 Lyon, France*
[4]*Institut Jean Le Rond d'Alembert (UMR 7190), CNRS, Sorbonne Universités, 75005 Paris, France*
[5]*Department of Physics, North Carolina State University, Raleigh, North Carolina 27607, USA*
[6]*Univ. Grenoble Alpes, CNRS, ISTerre, 38000 Grenoble, France*

(Received 8 March 2018; revised manuscript received 12 December 2018)

The Mohr-Coulomb criterion is widely used in geosciences and solid mechanics to relate the state of stress at failure to the observed orientation of the resulting faults. This relation is based on the assumption that macroscopic failure takes place along the plane that maximizes the Coulomb stress. Here, this hypothesis is assessed by simulating compressive tests on an elastodamageable material that follows the Mohr-Coulomb criterion at the mesoscopic scale. We find that the macroscopic fault orientation is not given by the Mohr-Coulomb criterion. Instead, for a weakly disordered material, it corresponds to the most unstable mode of damage growth, which we determine through a linear stability analysis of its homogeneously damaged state. Our study reveals that compressive failure emerges from the coalescence of damaged clusters within the material and that this collective process is suitably described at the continuum scale by introducing an elastic kernel that describes the interactions between these clusters.

DOI:

In 1773, Charles-Augustin de Coulomb proposed his celebrated failure criterion for materials loaded under shear or compression [1]. He postulated that failure occurs along a fault plane when the applied shear stress τ acting on that plane overcomes a resistance consisting of two parts of different nature: a cohesion τ_c, which can be interpreted as an intrinsic shear strength of the material, and a resistance proportional to the normal pressure, σ_N. This results in the Mohr-Coulomb (MC) failure criterion:

$$|\tau| = \tau_c + \mu\sigma_N. \tag{1}$$

Following the former work of Amontons [2], this dependence upon pressure led Coulomb to call it *friction*, with μ the corresponding friction coefficient and $\phi = \tan^{-1}(\mu)$ the angle of internal friction. As a consequence, faulting should occur along the plane that maximizes the Coulomb's stress $|\tau| - \mu\sigma_N$. Its orientation with respect to the maximum principal compressive stress is given by the MC angle

$$\theta_{\mathrm{MC}} = \frac{\pi}{4} - \frac{\phi}{2}. \tag{2}$$

This work led to the so-called Anderson theory of faulting [3], which is widely used in geophysics to interpret the orientation of conjugate faults [4] and the orientation of faults with respect to tectonic forces [5]. In this theory, θ_{MC} is uniquely a function of the internal friction angle ϕ and hence is independent of confinement and dilatancy.

Solid mechanics models of compressive failure generally adopt the same point of view: fault formation is described as a localization instability in the constitutive inelastic response of the material [6,7]. As such, if the material behavior follows the Mohr-Coulomb criterion, the fault inclination observed at the macroscopic scale is expected to follow the MC angle prediction (2).

However, important issues remain to be addressed regarding the applicability of this theory. Even though the MC criterion (1) describes accurately the failure envelope of quasibrittle solids like rocks [8,9] and ice [10,11], the ability of MC angle prediction (2) to capture fault orientation is still debated [12,13]. In particular, experiments have reported an increase of the fault angle with the lateral confinement, which is incompatible with the MC prediction [14–16]. Besides, while Coulomb's theory provides a simple instantaneous criterion for failure, it says nothing about the process of damage spreading that precedes it. It is now widely accepted that the compressive failure of quasibrittle materials does not occur suddenly, but instead involves the nucleation and growth of microcracks, which interact and finally coalesce to form a macroscopic fault [21–23]. It is not clear at all if this phenomenology is compatible with the point of view that macroscopic faulting emerges from a local instability in the material constitutive response [3,6,7], nor with the assumption that fault orientation in materials that do follow the MC failure criterion is given by the MC angle.

Damage spreading under compression and the progression towards macroscopic failure is well captured by continuum damage models, wherein microcrack density at the mesoscopic scale is represented by a damage variable and is coupled to the elastic modulus of the material [24–27] (Fig. 1). In these models, a failure criterion is implemented at the local scale, that is, usually, the scale of the mesh grid element. Material heterogeneity is accounted for by introducing some noise in either the elastic modulus or the local failure criterion. When the state of stress over a given element exceeds this criterion, the level of damage of this element increases, thereby decreasing its elastic modulus. Long-range elastic interactions arise from the stress redistribution initiated by the local drop in the elastic modulus. This redistribution can induce damage growth in neighboring elements and eventually trigger avalanches of damaging events over longer distances. Such models have been shown to reproduce many features of brittle compressive failure, such as the clustering of rupture events and the power-law distribution of acoustic event sizes prior to the emergence of a macroscopic fault [24,28–30]. They are thus relevant tools to study the process of damage localization that leads to failure and, in particular, the dependence of the angle of localization of damage on the parameters involved in the damage criteria.

Here, we use such a tool to investigate how the macroscopic fault emerges from the accumulation of microscopic damage events and test commonly used models that describe compressive failure as a local material instability [6,7]. In particular, we simulate compression experiments of specimens of an elastodamageable material that satisfy the MC failure criterion at the mesoscopic scale and study the inclination of the macroscopic rupture plane as a function of the internal friction angle under different confinement conditions. We show that the orientation of the simulated fault is not given by the MC angle. Instead, we find that the most unstable mode of damage growth, which is inferred from a linear stability analysis at the specimen scale, provides a good estimation of the fault orientation for weakly heterogeneous materials. Our findings shed light on the significance of elastic interactions and damage coalescence on the fault formation during compressive failure of quasi-brittle materials. It also suggests that the modeling strategy that consists in damage localization from the homogenized material response may be insufficient, but that this difficulty may be overcome by addressing the stability of the damage growth process at the macroscopic scale using the elastic interaction kernel introduced in this study.

Following Refs. [26,28] and others, the model is based on an isotropic linear-elastic constitutive law where the elastic modulus,

$$E(d) = (1 - d)E^0, \qquad (3)$$

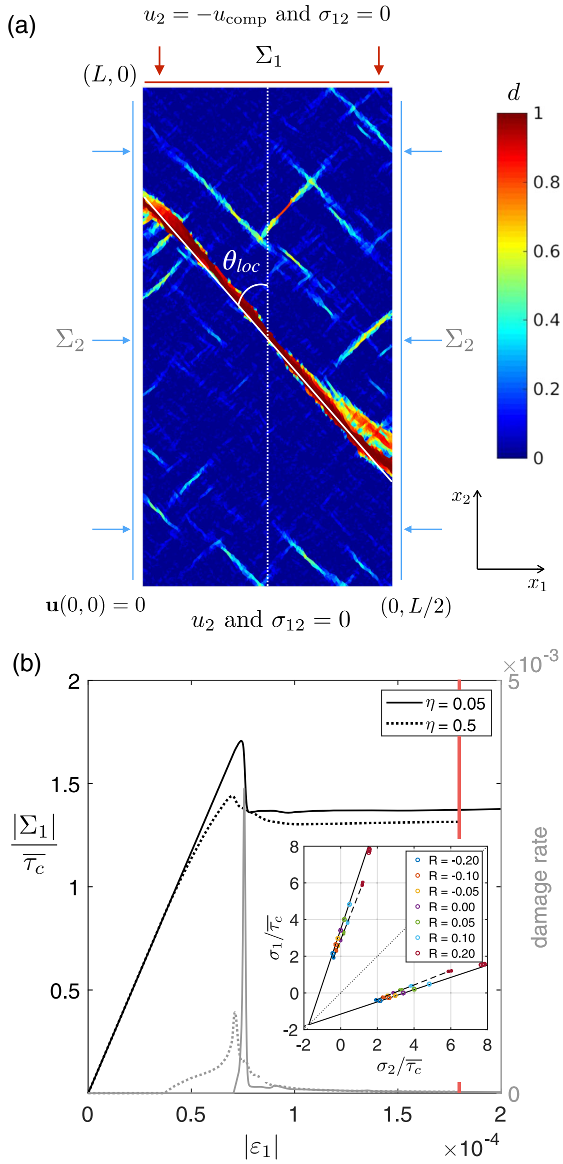

FIG. 1. Compressive test simulation. (a) The prescribed boundary conditions are superimposed to a snapshot of the field of the level of damage d simulated after peak load [timing indicated by the red vertical line in (b)]. The material properties in this simulation are $\phi = 30°$ and $\nu = 0.3$ and the disorder parameters, $\eta = 0.05$ and $a = 1$. No lateral confinement is applied. The orientation of the fault θ_{loc} is determined by a projection histogram method [16]. (b) The corresponding stress-strain (black) and damage rate (gray) curves are given by the solid lines. The dotted lines show the same quantities for a simulation using identical loading and material properties and a stronger disorder ($\eta = 0.5$ and $a = 1$). [(b), inset] Macroscopic maximum and minimum principal stresses, Σ_1, Σ_2, (colored dots) estimated at the onset of damage localization (i.e., at peak load) in a set of 5 simulations using the same material properties as in (a) and (b) and different confining ratios (biaxial compression for $R > 0$ and biaxial compression tension for $R < 0$). The black solid lines represent the MC criterion for a homogeneous material with cohesion $\bar{\tau}_c$. Open circles are used for the disorder parameters $\eta = 0.05$ and $a = 1$ and filled circles for the parameters $\eta = 0.5$ and $a = 1$.

is a decreasing function of the scalar internal variable, $d \in [0, 1]$, which describes the level of damage in a material element, with E^0 the Young's modulus of the undamaged specimen. For sake of simplicity, Poisson's ratio ν is assumed constant and does not vary with d. Material heterogeneities are introduced via the local critical strength by assigning different cohesions τ_c to the constitutive material elements. In the present simulations, we use $E^0 = 50$ MPa and $\bar{\tau}_c = 25$ kPa. We checked that these specific values do not affect our results as long as $\bar{\tau}_c \ll E^0$ [16].

In the numerical simulations, a two-dimensional rectangular specimen of an elastodamageable material with dimensions $L \times L/2$ is compressed with a stress Σ_1 by prescribing a constant velocity u_{comp} on its upper short edge with the opposite edge fixed in the direction of the forcing [Fig. 1(a)]. Plane stresses are assumed. A confining stress Σ_2 can be applied on the lateral sides; in this case, the confinement ratio $R = \Sigma_2/\Sigma_1$ is kept constant. We denote $\boldsymbol{\sigma}^0$ the external stress tensor prescribed to the sample. At each time step, the damage level of the material elements for which the stress is overcritical with respect to the local MC criterion is increased such that overcritical stresses are projected back onto the MC envelope [16]. Both the prescribed velocity on the upper edge of the specimen and the lateral confinement are small enough to ensure a quasistatic driving and small deformations. The simulations therefore rely on the numerical resolution of the following force balance and Hooke's law:

$$\nabla \cdot \boldsymbol{\sigma}(\boldsymbol{r}) = 0, \tag{4}$$

$$\boldsymbol{\sigma}(\boldsymbol{r}) = \frac{E}{1+\nu}\boldsymbol{\epsilon}(\boldsymbol{r}) + \frac{E\nu}{1-\nu^2}\mathrm{tr}[\boldsymbol{\epsilon}(\boldsymbol{r})]\mathbf{1}, \tag{5}$$

where $\boldsymbol{\sigma}(\boldsymbol{r})$ and $\boldsymbol{\epsilon}(\boldsymbol{r})$ are the planar stress and strain tensors in the specimen.

Equations (4) and (5) are solved using variational methods on a two-dimensional amorphous grid made of more than 33 000 triangular elements [16]. A typical stress-strain response is shown in Fig. 1(b) for no confinement, $\phi = 30°$ and $\nu = 0.3$. Consistent with the failure in compression of quasibrittle materials monitored via acoustic emissions [30,31] as well as with previous progressive damage simulations of this process [26], the simulated damage indicates some precursory activity. It is initially distributed homogeneously over the domain (not shown) and localizes progressively as the loading is increased. Fault formation is identified by the sudden rise of the damage rate and corresponds to peak load.

As done in laboratory experiments on rocks [13,15] and ice [10], we measured the failure envelope by testing specimens under different confinement ratios [see inset of Fig. 1(b)]. We observe that the failure envelope of the specimen given by the principal stresses (Σ_1, Σ_2) at peak load reproduces the MC criterion enforced at the material level. Therefore, in agreement with observations [11], μ appears to be a scale-independent property in our numerical model.

The damage field after peak load exhibits a localization band characteristic of compressive failure [Fig. 1(a)]. A projection histogram method is used to determine its orientation [16], hereinafter referred to as the localization angle, θ_{loc}. We observe that the value of θ_{loc} is robust and independent of both the mesh size and the aspect ratio of the specimen [16]. A first set of compression test simulations representing a minimum disorder scenario is initialized with a field of cohesion that is uniform for all except one element chosen at random. For this inclusion, τ_c is initially 5% weaker and is reset to the uniform value of its neighbors after its first damage event. Figure 2(a) shows the mean localization angle as a function of the internal friction angle ϕ and Figs. 2(b), 2(c), the same results for different Poisson's and confinement ratios, respectively. Neither the value nor the variation of θ_{loc} with ϕ agree with the MC prediction. In particular, the simulated fault orientation varies with Poisson's ratio as well as with confinement, a

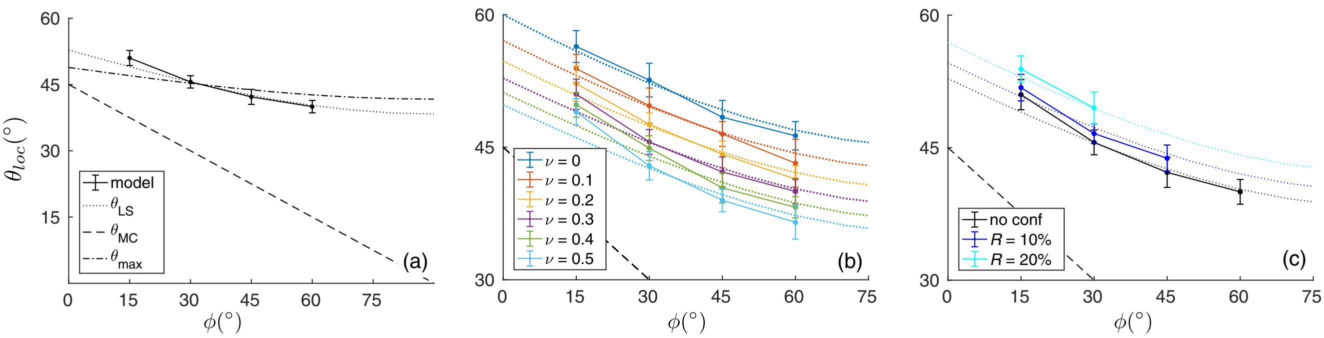

FIG. 2. (a) Mean localization angle θ_{loc} as a function of the internal friction angle ϕ for an ensemble of 25 simulations with minimal disorder using identical boundary and loading conditions. No confinement is applied and $\nu = 0.3$. The black dashed line shows the MC prediction θ_{MC}, the dotted line, the angle of the most unstable mode θ_{LS}, and the dashed-dotted line the angle of maximal stress redistribution θ_{max}. The error bars represent ±1 standard deviation from the mean. Mean localization angle for (b) different values of Poisson's ratio without confinement and (c) different values of confinement ratio for $\nu = 0.3$.

dependence that is not accounted for in the MC theory, but that has been observed in laboratory experiments on rocks [13–15].

To understand how macroscopic failure arises in the model, we perform a linear stability analysis of the homogeneously damaged solution. In our simulations, the damage field follows the evolution law,

$$\frac{\partial d}{\partial t}(\boldsymbol{r},t) = F[\boldsymbol{\sigma}^0, d(\boldsymbol{r},t)], \tag{6}$$

where the damage driving force F is nonlocal: its value for a material element depends on the damage level everywhere in the specimen. The linear stability analysis amounts to linearizing this evolution equation around an homogeneous damage field. Assuming an infinite specimen, the problem is translation invariant and the linearization can be written as a convolution product of the damage field with the elastic kernel $\Psi_{\boldsymbol{\sigma}^0,d^0}$ [32]:

$$F[\boldsymbol{\sigma}^0, d(\boldsymbol{r},t)] \simeq F[\boldsymbol{\sigma}^0, d^0] + \Psi_{\boldsymbol{\sigma}^0,d^0} * \delta d(\boldsymbol{r},t), \tag{7}$$

where $\delta d(\boldsymbol{r},t) = d(\boldsymbol{r},t) - d^0 \ll 1$. The kernel Ψ is reminiscent of the Eshelby solution for the mechanical field around a soft inclusion embedded in an infinite 2D elastic medium, which also decays as $1/r^2$ [33]. It provides the redistribution of the driving force F following a localized (δ-distributed) damage growth and as such, describes the elastic interactions between material elements during damage spreading. In Fourier space, it does not depend on the magnitude of the wave vector $\boldsymbol{q}$, but only on its polar angle, ω [16]:

$$\tilde{\Psi}(\omega) = A\left(\sin(\omega)^2 - \frac{1+\sin(\phi)}{2}\right)[\delta - \sin(\omega)^2], \tag{8}$$

with $A = 2\Sigma_1\{[(1-\nu)(1-R)]/(1-d^0)\}$ and $\delta = (\nu - R)/[(1+\nu)(1-R)]$. The evolution of the damage field perturbations is inferred from Eqs. (6), (7). Considering harmonic modes $\delta d(\boldsymbol{r}) \propto \cos(\boldsymbol{q}\cdot\boldsymbol{r})$, their growth rate is given by $\tilde{\Psi}(\omega)$. Since the kernel is maximal and positive for $\sin(\omega^*)^2 = [1+\sin(\phi)+2\delta]/4$, one concludes that (i) a homogeneous damage field is unstable and (ii) all the wave vectors with the orientation ω^* diverge at the same rate as $\tilde{\Psi}$ is independent of the magnitude of the wave vector. Hence, any linear combination of these modes also diverges at the same rate, corresponding to a localization band that is perpendicular to $\boldsymbol{q}$, leading to an inclination $\theta_{\mathrm{LS}} = \pi/2 \pm \omega^*$ or

$$\theta_{\mathrm{LS}} = \arccos\left(\frac{\sqrt{1+\sin(\phi)+2\delta}}{2}\right), \tag{9}$$

with respect to the direction of maximum principal compressive stress. For the sake of simplicity, only the solution lying in $[0,\pi/2]$ is kept here, but both inclinations are actually possible in agreement with the orientation of the secondary faults observed in Fig. 1(a).

We compare the predicted inclination θ_{LS} with the localization angle θ_{loc} from the simulations. We find that the prediction is in excellent agreement with the results of the minimal disorder numerical simulations [Fig. 2(a)] and reproduces the observed dependence on Poisson's ratio [Fig. 2(b)]. The increase of θ_{loc} with confinement [Fig. 2(c)] is also well captured, in qualitative agreement with experimental observations [15,16].

Alternatively, the fault orientation may be compared to the direction along which stress redistribution is maximal after a damage event [34]. This angle, $\theta_{\max} = \arccos\{\sqrt{[3+\sin(\phi)+2\delta]/8}\}$, which maximizes the angular part of the elastic kernel in real space [16], is significantly different from the orientation of the most unstable mode, θ_{LS}. Recent compression experiments on granular materials [35,36] have suggested that $\theta_{\max}$ may correspond to the preferred orientation of the precursory damage cascades prior to failure while θ_{LS} provides the final macroscopic fault inclination. As shown in Fig. 2(a), θ_{LS} clearly provides a better agreement with the simulations than $\theta_{\max}$ in the case of a single evanescent heterogeneity.

Real and, especially, natural materials are heterogeneous and comprise many randomly distributed impurities that can serve as local stress concentrators, initiating microcracking and leading to an extended regime of diffuse damage growth prior to localization [21,23,37,38]. To determine if and how this regime affects the final orientation of the macroscopic fault, we introduce disorder in the critical strength by drawing randomly the cohesion of a proportion a of the material elements in the range $\bar{\tau}_c[1-\eta, 1+\eta]$, with the cohesion of the remaining proportion $1-a$ of the elements set to the average cohesion, $\bar{\tau}_c$. We consider cases of weak [$\eta = 0.05$, Fig. 3(a)] and strong [$\eta = 0.5$, Fig. 3(b)] disorder. In both cases, the value of a is varied between 10^{-4}, corresponding to a few ($\simeq 3$) inclusions in a homogeneous matrix, and $a = 1$, for which all elements have a different critical strength. Consistent with the minimum disorder case investigated above, the agreement with the orientation obtained from the linear stability analysis, θ_{LS}, is best for $a = 10^{-4}$ [Figs. 3(a), 3(b)]. The deviation from θ_{LS} increases with both the density a of inclusions and the strength η of the disorder, indicating that disorder significantly affects the fault orientation θ_{loc}. In all cases however, θ_{loc} remains well above θ_{MC}, and a clear dependence on Poisson's ratio and on confinement is still observed [see Figs. 3(c), 3(d)]. These departures from the MC theory are in qualitative agreement with the experimental observations reporting the localization angle and its dependence on confinement [10,13–16]. As a direct consequence, our findings question the estimation of internal friction or of applied stresses from faults orientation in natural settings [3–5]. To go further in the comparison of

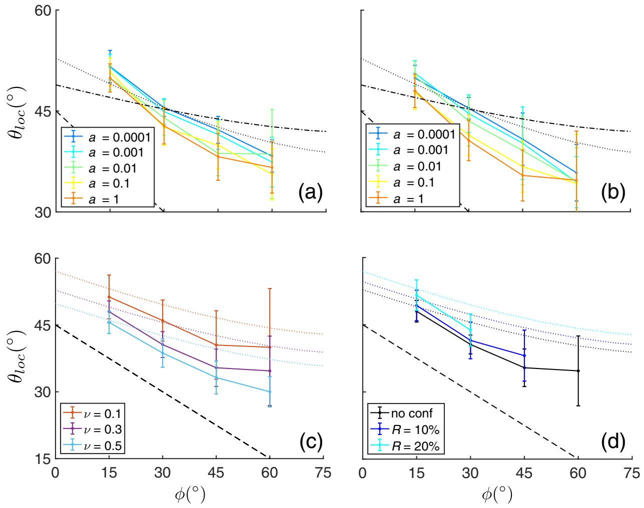

FIG. 3. Localization angle measured from the compression simulations as a function of the internal friction angle for (a) weak disorder ($\eta = 0.05$) and (b) strong disorder ($\eta = 0.5$) and different values of a. No confinement is applied and $\nu = 0.3$. Mean $\theta_{\rm loc}$ for $a = 1$ and $\eta = 0.5$ (strong disorder) and (c) different values of ν without confinement and (d) different confinement ratios for $\nu = 0.3$. The maximum confinement ratio, $R_{\max}$ [16], is 58% for $\phi = 15°$, 33% for $\phi = 30°$, 17% for $\phi = 45°$, and 7% for $\phi = 60°$. The black dashed line shows $\theta_{\rm MC}$, the dotted lines $\theta_{\rm LS}$, and the dashed-dotted line $\theta_{\max}$.

experimental observations with the newly developed theory, triaxial loading as well as a possible dependence of Poisson's ratio on damage should be introduced.

To conclude, the discrepancy between the fault angle and the Mohr-Coulomb prediction indicates that compressive failure, even when it is not preceded by an extended regime of stable damage growth, results from the *collective* spreading of damage within the specimen. As such, the fault angle observed in our simulations is successfully captured from a stability analysis performed at the *macroscopic* scale. The role of elasticity, which is responsible for the redistribution of the stress after a damage event and for interactions between microcracks, reflects in the dependence of the localization angle on the Poisson's ratio. The fact that the MC criterion, derived from the stability of a single material element, fails to predict the fault angle suggests commonly used modeling approaches to compressive failure [6,7] that do not account for the long-range elastic interactions between damage events may not predict accurately the localization threshold, the resulting band inclination, and their relation with the material and loading parameters.

V. D. is supported by TOTAL S. A. E. B. and L. P. are supported by the Emergence from Sorbonne Universités. We thank D. Kondo and A. Rosso for enlightening discussions and A. Amon for providing codes for the projection histogram calculations.

[1] C. A. Coulomb, Essai sur une application des règles de maximis et minimis à quelques problèmes de statique relatifs à l'architecture, Mém. Math. Phys. **7**, 343 (1773).
[2] G. Amontons, *Mémoires de l'Académie Royale* (J. Boudot, Paris, 1699) Chap. De la résistance causée dans les machines (About resistance and force in machines), pp. 257–282.
[3] E. M. Anderson, The dynamics of faulting, Trans. Edinburgh Geol. Soc. **8**, 387 (1905).
[4] E. M. Schulson, Compressive shear faults within arctic sea ice: Fractures on scales large and small, J. Geophys. Res. **109** (2004).
[5] Z. Reches, Determination of the tectonic stress tensor from slip along faults that obey the coulomb yield condition, Tectonics **6**, 849 (1987).
[6] J. W. Rudnicki and J. R. Rice, Conditions for the localization of deformation in pressure-sensitive dilatant materials, J. Mech. Phys. Solids **23**, 371 (1975).
[7] D. Bigoni, *Nonlinear Solid Mechanics: Bifurcation Theory and Material Instability* (Cambridge University Press, Cambridge, England, 2012).
[8] J. D. Byerlee, Frictional characteristics of granite under high confining pressure, J. Geophys. Res. **72**, 3639 (1967).
[9] J. C. Jaeger and N. G. W. Cook, *Fundamentals of Rock Mechanics* (Chapman and Hall, Cambridge, 1979).
[10] E. M. Schulson, A. L. Fortt, D. Iliescu, and C. E. Renshaw, On the role of frictional sliding in the compressive fracture of ice and granite: Terminal vs post-terminal failure, Acta Mater. **54**, 3923 (2006).
[11] J. Weiss and E. M Schulson, Coulombic faulting from the grain scale to the geophysical scale: Lessons from ice, J. Phys. D **42**, 214017 (2009).
[12] J. P. Bardet, A comprehensive review of strain localization in elastoplastic soils, Computers and Geotechnics **10**, 163 (1990).
[13] A. Hackston and E. Rutter, The Mohr–Coulomb criterion for intact rock strength and friction—a re-evaluation and consideration of failure under polyaxial stresses, Solid Earth **7**, 493 (2016).
[14] A. Haied, D. Kondo, and J. P. Henry, Strain localization in Fontainebleau sandstone, Mech. Cohes.-Frict. Mater **5**, 239 (2000).
[15] B. Haimson and J. W. Rudnicki, The effect of the intermediate principal stress on fault formation and fault angle in siltstone, J. Struct. Geol. **32**, 1701 (2010), fault Zones.
[16] See Supplemental Material at http://link.aps.org/supplemental/10.1103/PhysRevLett.000.000000 for more details, which includes Refs. [17–20].
[17] P. Saramito, *Efficient C++ finite element computing with Rheolef* (CNRS-CCSD ed., 2015), http://cel.archives-ouvertes.fr/cel-00573970.
[18] C. Geuzaine and J.-F. Remacle, Gmsh: A 3-d finite element mesh generator with built-in pre- and post-processing facilities, Int. J. Numer. Methods Eng. **79**, 1309 (2009).
[19] R. O. Duda and P. E. Hart, Use of the hough transformation to detect lines and curves in pictures, Commun. ACM **15**, 11 (1972).
[20] R. Lehoucq, J. Weiss, B. Dubrulle, A. Amon, A. Le Bouil, J. Crassous, and D. Amitrano, Analysis of image vs position, scale and direction reveals pattern texture anisotropy, Front. Phys. **2**, 84 (2015).

[21] D. A. Lockner, J. D. Byerlee, V. Kuksenko, A. Ponomarev, and A. Sidorin, Quasi-static fault growth and shear fracture energy in granite, Nature (London) **350**, 39 (1991).

[22] *Rock Physics and Natural Hazards*, edited by J. Fortin, S. Stanchits, G. Dresen, and Y. Gueguen (Birkhäuser, Basel, 2009), p. 823.

[23] F. Renard, B. Cordonnier, M. Kobchenko, N. Kandula, J. Weiss, and W. Zhu, Microscale characterization of rupture nucleation unravels precursors to faulting in rocks, Earth Planet. Sci. Lett. **476**, 69 (2017).

[24] S. Zapperi, A. Vespignani, and H. E. Stanley, Plasticity and avalanche behaviour in microfracturing phenomena, Nature (London) **388**, 658 (1997).

[25] V. Lyakhovsky, Y. Ben-Zion, and A. Agnon, Distributed damage, faulting and friction, J. Geophys. Res. **102**, 27635 (1997).

[26] D. Amitrano, J.-R. Grasso, and D. Hantz, From diffuse to localised damage through elastic interaction, Geophys. Res. Lett. **26**, 2109 (1999).

[27] E. Berthier, V. Démery, and L. Ponson, Damage spreading in quasi-brittle disordered solids: I. Localization and failure, J. Mech. Phys. Solids **102**, 101 (2017).

[28] C. Tang, Numerical simulation of progressive rock failure and associated seismicity, Int. J. Rock Mech. Min. Sci. Geomech. Abstr. **34**, 249 (1997).

[29] L. Girard, D. Amitrano, and J. Weiss, Failure as a critical phenomenon in a progressive damage model, J. Stat. Mech. 2010, P01013 (2010).

[30] D. Amitrano, Brittle-ductile transition and associated seismicity: Experimental and numerical studies and relationship with the b value, J. Geophys. Res. **108**, 2044 (2003).

[31] S. J. D. Cox and P. G. Meredith, Microcrack formation and material softening in rock measured by monitoring acoustic emissions, Int. J. Rock Mech. Min. Sci. Geomech. Abstr. **30**, 11 (1993).

[32] J. Weiss, L. Girard, F. Gimbert, D. Amitrano, and D. Vandembroucq, (Finite) statistical size effects on compressive strength, Proc. Natl. Acad. Sci. U.S.A. **111**, 6231 (2014).

[33] J. D. Eshelby, The determination of the elastic field of an ellipsoidal inclusion, and related problems, Proc. R. Soc. A **241**, 376 (1957).

[34] A. Nicolas, E. E. Ferrero, K. Martens, and J. L. Barrat, Deformation and flow of amorphous solids: A review of mesoscale elastoplastic models, arXiv:1708.09194.

[35] A. Le Bouil, A. Amon, S. McNamara, and J. Crassous, Emergence of Cooperativity in Plasticity of Soft Glassy Materials, Phys. Rev. Lett. **112**, 246001 (2014).

[36] K. Karimi and J.-L. Barrat, Correlation and shear bands in a plastically deformed granular medium, Sci. Rep. **8**, 4021 (2018).

[37] Y. Tal, B. Evans, and U. Mok, Direct observations of damage during unconfined brittle failure of carrara marble, J. Geophys. Res. Solid Earth **121**, 1584 (2016).

[38] F. Renard, J. Weiss, J. Mathiesen, Y. Ben-Zion, N. Kandula, and B. Cordonnier, Critical evolution of damage toward system-size failure in crystalline rock, J. Geophys. Res. **123**, 1969 (2018).

Collective damage growth controls fault orientation in quasi-brittle compressive failure Supplemental material

Véronique Dansereau,[1] Vincent Démery,[2, 3] Estelle Berthier,[4, 5] Jérôme Weiss,[6] and Laurent Ponson[4]

[1] *Nansen Environmental and Remote Sensing Center, N-5006 Bergen, Norway*
[2] *Gulliver, CNRS, ESPCI Paris, PSL Research University, 10 rue Vauquelin, 75005 Paris, France*
[3] *Univ Lyon, ENS de Lyon, Univ Claude Bernard Lyon 1, CNRS, Laboratoire de Physique, F-69342 Lyon, France*
[4] *Institut Jean Le Rond d'Alembert (UMR 7190), CNRS, Sorbonne Universités, 75005 Paris, France*
[5] *Department of Physics, North Carolina State University, Raleigh, North Carolina 27607, USA*
[6] *Univ. Grenoble Alpes, CNRS, ISTerre, 38000 Grenoble, France*

I. EXPERIMENTAL DATA

A precise determination of the fault orientation ($\theta_{\rm loc}$, according to our notations) during compressive failure tests was rarely reported in the literature. Table I summarizes available experimental results on rocks and ice that allow comparing $\theta_{\rm loc}$ with the Mohr-Coulomb (MC) prediction, $\theta_{\rm MC}$. These were obtained from series of multiaxial compressive tests with varying levels of confinement. In this table, the corresponding MC prediction, $\theta_{\rm MC}$, was either reported directly by the authors [1, 2], or calculated from the reported values of Σ_1 (there, the macroscopic principal stress at failure, see Fig. 1 of the main text) and Σ_2 (macroscopic minimum principal stress or confining pressure) [3, 4]. In all cases, an excellent agreement with a linear relation of the form

$$\Sigma_1 = q\Sigma_2 + \sigma_c \tag{1}$$

is obtained, which corresponds to the macroscopic Mohr-Coulomb failure enveloppe in such 3d loading configuration. The angle of internal friction ϕ can therefore be calculated from:

$$\phi = \arcsin\left(\frac{q-1}{q+1}\right), \tag{2}$$

which yields $\theta_{\rm MC}$ from Eq. (2) of the main text.

From Table I, two results stand out:

- With the exception of siltstone under low confinements [1], Coulomb's prediction $\theta_{\rm MC}$ generally underestimates the observed fault angle $\theta_{\rm loc}$. It is worth noting that a similar conclusion was obtained from a compilation of data on soils [5].
- $\theta_{\rm loc}$ is generally observed to increase with increasing confinement, an evolution not accounted for by Coulomb's theory.

II. CALCULATION OF THE ELASTIC KERNEL

In our model, we assume that the damage field, d, follows the evolution law

$$\alpha\frac{\partial d}{\partial t}(\boldsymbol{r},t) = \max(Y(\boldsymbol{\sigma}(\boldsymbol{r})),0), \tag{3}$$

where $Y(\boldsymbol{\sigma})$ is a driving force that encodes the Mohr-Coulomb (MC) criterion:

$$Y(\boldsymbol{\sigma}) = \sigma_1 - \sigma_2 - (\sigma_1+\sigma_2)\sin(\phi) - 2\tau_{\rm c}\cos(\phi), \tag{4}$$

where $\sigma_1 > \sigma_2$ are the eigenvalues of $-\boldsymbol{\sigma}$ (they are positive for compression). The parameter α in this equation can be absorbed in a redefinition of the time, hence it is omitted in the following. Computing the elastic kernel amounts to linearizing Eq. (3) around a homogeneous damage field, i.e., assuming weak damage fluctuations, $d(\boldsymbol{r}) = d^0 + d^1(\boldsymbol{r})$, with d^0 the spatial average of the damage field.

A. Elastic moduli and damage driving force

First, we linearize the Lamé parameters:

$$G(d^0+d^1(\boldsymbol{r})) \simeq G(d^0) + G'(d^0)d^1(\boldsymbol{r}) = G^0[1+g^1(\boldsymbol{r})], \tag{5}$$

$$\lambda(d^0+d^1(\boldsymbol{r})) \simeq \lambda(d^0) + \lambda'(d^0)d^1(\boldsymbol{r}) = G^0[\ell^0+\ell^1(\boldsymbol{r})], \tag{6}$$

where we have defined

$$G^0 = G(d^0), \tag{7}$$

$$\ell^0 = \frac{\lambda(d^0)}{G(d^0)} = \frac{2\nu}{1-\nu}, \tag{8}$$

$$g^1(\boldsymbol{r}) = \frac{G'(d^0)}{G(d^0)}d^1(\boldsymbol{r}) = -\frac{d^1(\boldsymbol{r})}{1-d^0}, \tag{9}$$

$$\ell^1(\boldsymbol{r}) = \frac{\lambda'(d^0)}{G(d^0)}d^1(\boldsymbol{r}) = -\frac{\ell^0 d^1(\boldsymbol{r})}{1-d^0}. \tag{10}$$

Material/Experiment	Ref.	ϕ	$\theta_{\rm MC}$	$\theta_{\rm loc,min}$	$\theta_{\rm loc,max}$	Dependence of $\theta_{\rm loc}$ on confinement
Fontainebleau sandstone	[3]	49	20,5	29	32	Increases with confinement
Pennant sandstone	[4]	44	23	30	31	No trend
Darley Dale sandstone	[4]	34	28	24	36	Increases with confinement
Siltstone Core I	[1]	34.6	27.7	17	31	Increases with confinement
Siltstone Core II	[1]	30.3	29.9	14	38	Increases with confinement
Ice at $-3°$C	[2]	34	28	29	29	Not reported
Ice at $-10°$C	[2]	44	23	26	26	Not reported

TABLE I. Experimental measurements of the internal friction angle ϕ from the failure enveloppe, and range $[\theta_{\rm loc,min}, \theta_{\rm loc,max}]$ of localization angles for different values of the confinement, compared to the Mohr-Coulomb angle $\theta_{\rm MC}$ deduced from ϕ.

The last equation emerges from the fact that the Poisson ratio does not depend on damage, hence the ratio of the two Lamé parameters remains constant.

Second, we linearize the driving force for weak stress perturbations $\boldsymbol{\sigma}^1(\boldsymbol{r}) = \boldsymbol{\sigma}(\boldsymbol{r}) - \boldsymbol{\sigma}^0$, where $\boldsymbol{\sigma}^0$ is the external stress applied on the sample. If the eigenvalues of $-\boldsymbol{\sigma}^0$ are $\sigma_1 > \sigma_2$, to the first order in $\boldsymbol{\sigma}^1$, the eigenvalues of $-\boldsymbol{\sigma}$ are given by $\sigma_i - \sigma^1_{ii}$, $1 \le i \le 2$. The driving force (4) can thus be expanded as

$$\begin{aligned} Y(\boldsymbol{\sigma}^0 + \boldsymbol{\sigma}^1) &\simeq Y(\boldsymbol{\sigma}^0) - \sigma^1_{11} + \sigma^1_{22} + (\sigma^1_{11} + \sigma^1_{22})\sin(\phi) \\ &= Y(\boldsymbol{\sigma}^0) + \boldsymbol{\upsilon} : \boldsymbol{\sigma}^1, \end{aligned} \tag{11}$$

where the colon denotes the contraction, $\boldsymbol{\upsilon} : \boldsymbol{\sigma}^1 = \upsilon_{ij}\sigma^1_{ij}$ (summation over repeated indices is assumed), and

$$\boldsymbol{\upsilon} = \begin{pmatrix} -1 + \sin(\phi) & 0 \\ 0 & 1 + \sin(\phi) \end{pmatrix}. \tag{12}$$

B. Stress distribution due to heterogeneous elastic moduli

Here, we compute the stress variations, $\boldsymbol{\sigma}^1(\boldsymbol{r})$, as a function of the variations in the elastic moduli, $g^1(\boldsymbol{r})$ and $\ell^1(\boldsymbol{r})$ (Eqs. (5, 6)), assuming an infinite domain. We use the same notation for the stress, $\boldsymbol{\sigma}(\boldsymbol{r})$, the strain, $\boldsymbol{\epsilon}(\boldsymbol{r})$, and the displacement, $\boldsymbol{u}(\boldsymbol{r})$: the quantity with exponent 0 refers to the zeroth order term, which corresponds to the homogeneous solution, and the quantity with exponent 1 refers to its perturbations.

We expand the elasticity equations to the first order — discarding second order terms of the form $g^1(\boldsymbol{r})u^1(\boldsymbol{r})$— and write it in components form as

$$\partial_i \sigma^1_{ij} = 0, \tag{13}$$

$$\frac{\sigma^1_{ij}}{G^0} = 2g^1\epsilon^0_{ij} + \ell^1\epsilon^0_{kk}\delta_{ij} + \partial_i u^1_j + \partial_j u^1_i + \ell^0\partial_k u^1_k \delta_{ij}, \tag{14}$$

where we drop the argument $\boldsymbol{r}$ of the different fields to simplify the writing and use the definition of the first order variations of the strain: $\epsilon^1_{ij} = (\partial_i u^1_j + \partial_j u^1_i)/2$.

We substitute for σ^1_{ij} (Eq. (14)) in Eq. (13) and obtain

$$\partial_i\partial_i u^1_j + \left(1 + \ell^0\right)\partial_j\partial_i u^1_i = -2(\partial_j g^1)\epsilon^0_{ij} - (\partial_j \ell^1)\epsilon^0_{ii}. \tag{15}$$

This equation can be solved in Fourier space, the Fourier transform of a function $f(\boldsymbol{r})$ being defined by

$$\tilde{f}(\boldsymbol{q}) = \int f(\boldsymbol{r})\mathrm{e}^{-\mathrm{i}\boldsymbol{q}\cdot\boldsymbol{r}}\mathrm{d}\boldsymbol{r}. \tag{16}$$

The derivatives then become $\partial_i \to \mathrm{i}q_i$ and we obtain

$$q^2\tilde{u}^1_j + \left(1 + \ell^0\right) q_j q_i \tilde{u}^1_i = 2\mathrm{i}\tilde{g}^1 q_i \epsilon^0_{ij} + \mathrm{i}\tilde{\ell}^1 q_j \epsilon^0_{ii}. \tag{17}$$

Multipliying Eq. (17) by q_j, we obtain

$$q^2(2 + \ell^0)q_j\tilde{u}^1_j = 2\mathrm{i}\tilde{g}^1 q_i q_j \epsilon^0_{ij} + \mathrm{i}\tilde{\ell}^1 q^2 \epsilon^0_{ii}, \tag{18}$$

hence

$$q_j\tilde{u}^1_j = \frac{\mathrm{i}}{2 + \ell^0}\left(2\tilde{g}^1\frac{q_i q_j}{q^2}\epsilon^0_{ij} + \tilde{\ell}^1\epsilon^0_{ii}\right). \tag{19}$$

Using this expression in Eq. (17), we now get

$$\begin{aligned} \tilde{u}^1_j &= 2\mathrm{i}\tilde{g}^1\frac{q_i}{q^2}\epsilon^0_{ij} \\ &+ \mathrm{i}\frac{q_j}{q^2}\left(-2\frac{1+\ell^0}{2+\ell^0}\tilde{g}^1\frac{q_i q_k}{q^2}\epsilon^0_{ik} + \frac{1}{2+\ell^0}\tilde{\ell}^1\epsilon^0_{ii}\right). \end{aligned} \tag{20}$$

Inserting Eq. (20) in Eq. (14), the stress reads:

$$\frac{\tilde{\sigma}^1_{ij}}{G_0} = 2\tilde{g}^1\epsilon^0_{ij} + \tilde{\ell}^1\epsilon^0_{kk}\delta_{ij} + \mathrm{i}(q_i\tilde{u}^1_j + q_j\tilde{u}^1_i) + \mathrm{i}\ell^0 q_k\tilde{u}^1_k\delta_{ij} \tag{21}$$

$$= 2\tilde{g}^1\left(\epsilon^0_{ij} - \frac{q_iq_k\epsilon^0_{kj} + q_jq_k\epsilon^0_{ki}}{q^2} + \frac{1}{2+\ell^0}\frac{q_kq_l}{q^2}\epsilon^0_{kl}\left[2(1+\ell^0)\frac{q_iq_j}{q^2} - \ell^0\delta_{ij}\right]\right) + \frac{2\tilde{\ell}^1}{2+\ell^0}\epsilon^0_{kk}\left(\delta_{ij} - \frac{q_iq_j}{q^2}\right). \tag{22}$$

We can rewrite this expression in tensorial form using the tensor

$$Q_{ij}(\boldsymbol{q}) = \frac{q_iq_j}{q^2}, \tag{23}$$

which satisfies $\boldsymbol{Q}\cdot\boldsymbol{q} = \boldsymbol{q}$, $\boldsymbol{Q}\cdot\boldsymbol{Q} = \boldsymbol{Q}$ and $\boldsymbol{Q}:\mathbf{1} = 1$ (we denote $[\boldsymbol{A}\cdot\boldsymbol{B}]_{ij} = A_{ik}B_{kj}$). This leads to

$$\frac{\tilde{\boldsymbol{\sigma}}^1}{G^0} = 2\tilde{g}^1\left(\boldsymbol{\epsilon}^0 - \boldsymbol{Q}\cdot\boldsymbol{\epsilon}^0 - \boldsymbol{\epsilon}^0\cdot\boldsymbol{Q} + \frac{1}{2+\ell^0}\boldsymbol{Q}:\boldsymbol{\epsilon}^0\left[2(1+\ell^0)\boldsymbol{Q} - \ell^0\mathbf{1}\right]\right) + \frac{2\tilde{\ell}^1}{2+\ell^0}(\mathbf{1}:\boldsymbol{\epsilon}^0)(\mathbf{1}-\boldsymbol{Q}). \tag{24}$$

This last expression can be further simplified by using the property $(\boldsymbol{Q}:\boldsymbol{\sigma}^0)\boldsymbol{Q} = \boldsymbol{Q}\cdot\boldsymbol{\sigma}^0\cdot\boldsymbol{Q}$ and the Oseen tensor

$$\boldsymbol{O}(\boldsymbol{q}) = \mathbf{1} - \boldsymbol{Q}(\boldsymbol{q}), \tag{25}$$

which is the projector on the plane orthogonal to $\boldsymbol{q}$. Doing so, we obtain

$$\frac{\tilde{\boldsymbol{\sigma}}^1}{G^0} = 2\tilde{g}^1\left(\boldsymbol{O}\cdot\boldsymbol{\epsilon}^0\cdot\boldsymbol{O} + \frac{\ell^0}{2+\ell^0}(\boldsymbol{O}:\boldsymbol{\epsilon}^0)\boldsymbol{O}\right) + \frac{2(\tilde{\ell}^1 - \ell^0\tilde{g}^1)}{2+\ell^0}(\mathbf{1}:\boldsymbol{\epsilon}^0)\boldsymbol{O}. \tag{26}$$

Using the property $\ell^1 = \ell^0 g^1$, the last term cancels out and the expression reads:

$$\frac{\tilde{\boldsymbol{\sigma}}^1}{G^0} = 2\tilde{g}^1\left(\boldsymbol{O}\cdot\boldsymbol{\epsilon}^0\cdot\boldsymbol{O} + \frac{\ell^0}{2+\ell^0}(\boldsymbol{O}:\boldsymbol{\epsilon}^0)\boldsymbol{O}\right). \tag{27}$$

The final step consists in expressing the stress variations, $\tilde{\boldsymbol{\sigma}}^1$, as a function of the external uniform stress, $\boldsymbol{\sigma}^0$ We invert Hooke's law

$$\boldsymbol{\epsilon}^0 = \frac{1}{2G^0}\left[\boldsymbol{\sigma}^0 - \frac{\ell^0}{2(1+\ell^0)}(\mathbf{1}:\boldsymbol{\sigma}^0)\mathbf{1}\right] \tag{28}$$

and insert it into Eq. (22):

$$\tilde{\boldsymbol{\sigma}}^1 = \tilde{g}^1\left(\boldsymbol{O}\cdot\boldsymbol{\sigma}^0\cdot\boldsymbol{O} - \frac{\ell^0}{2+\ell^0}[(\mathbf{1}-\boldsymbol{O}):\boldsymbol{\sigma}^0]\boldsymbol{O}\right). \tag{29}$$

We note that $\boldsymbol{q}\cdot\boldsymbol{O} = 0$, which implies $\boldsymbol{q}\cdot\tilde{\boldsymbol{\sigma}}^1 = 0$, thus satisfying the equilibrium condition.

C. Elastic kernel, most unstable direction and θ_{LS}

Combining Eqs. (9, 10, 11, 29), we obtain the variations of the damage driving force $Y^1(\boldsymbol{r}) = Y(\boldsymbol{\sigma}(\boldsymbol{r})) - Y(\boldsymbol{\sigma}^0)$ in Fourier space:

$$\tilde{Y}^1(\boldsymbol{q}) \simeq \boldsymbol{v}:\tilde{\boldsymbol{\sigma}}^1(\boldsymbol{q}) \tag{30}$$

$$= \tilde{g}^1(\boldsymbol{q})\boldsymbol{v}:\left(\boldsymbol{O}\cdot\boldsymbol{\sigma}^0\cdot\boldsymbol{O} - \frac{\ell^0}{2+\ell^0}[(\mathbf{1}-\boldsymbol{O}):\boldsymbol{\sigma}^0]\boldsymbol{O}\right) \tag{31}$$

$$= \tilde{\Psi}(\boldsymbol{q})\tilde{d}^1(\boldsymbol{q}), \tag{32}$$

where we have defined the elastic kernel

$$\tilde{\Psi}(\boldsymbol{q}) = \frac{-1}{1-d^0} \times \boldsymbol{v}:\left(\boldsymbol{O}\cdot\boldsymbol{\sigma}^0\cdot\boldsymbol{O} - \frac{\ell^0}{2+\ell^0}[(\mathbf{1}-\boldsymbol{O}):\boldsymbol{\sigma}^0]\boldsymbol{O}\right). \tag{33}$$

The tensor products in the expression (33) for the kernel can be computed to obtain an explicit expression. The stress applied on the sample is given by

$$\boldsymbol{\sigma}^0 = -\Sigma_1\begin{pmatrix}1 & 0\\ 0 & R\end{pmatrix}, \tag{34}$$

where $\Sigma_1 > 0$ and R is the confinement ratio ($|R| < 1$). Denoting ω the polar angle of the wavevector $\boldsymbol{q}$, the Oseen tensor reads

$$\boldsymbol{O}(\omega) = \begin{pmatrix}\sin(\omega)^2 & -\sin(\omega)\cos(\omega)\\ -\sin(\omega)\cos(\omega) & \cos(\omega)^2\end{pmatrix}. \tag{35}$$

The kernel (33) can thus be expressed as

$$\tilde{\Psi}(\omega) = \alpha \left[\beta - \sin(\omega)^2\right] \left[\sin(\omega)^2 - \delta\right], \tag{36}$$

where

$$\alpha = \frac{2\Sigma_1(1-R)}{1-d^0}\left(1 + \frac{\ell^0}{2+\ell^0}\right), \tag{37}$$

$$\beta = \frac{1+\sin(\phi)}{2}, \tag{38}$$

$$\delta = \frac{\frac{\ell^0}{2+\ell^0} - R}{\left(1 + \frac{\ell^0}{2+\ell^0}\right)(1-R)} = \frac{\nu - R}{(1+\nu)(1-R)}. \tag{39}$$

It is maximal and positive for

$$\sin(\omega^*)^2 = \frac{\beta+\delta}{2} = \frac{1+\sin(\phi)+2\delta}{4}. \tag{40}$$

This provides the most unstable mode of damage growth that defines the *most unstable direction*

$$\theta_{\mathrm{LS}} = \arccos\left(\frac{\sqrt{1+\sin(\phi)+2\delta}}{2}\right) \tag{41}$$

with respect to the direction of maximum principal stress (direction 1).

D. Elastic kernel in real space and $\theta_{\max}$

Reintroducing the wavevector $\boldsymbol{q} = (q_x, q_y)$ in the expression (36) of the kernel, we obtain

$$\tilde{\Psi}(\boldsymbol{q}) = \alpha\left(\beta - \frac{q_y^2}{q^2}\right)\left(\frac{q_y^2}{q^2} - \delta\right) \tag{42}$$

$$= \alpha \frac{-\beta\delta q_x^4 + (\beta+\delta-2\beta\delta)q_x^2 q_y^2 + (\beta-1)(1-\delta)q_y^4}{q^4}. \tag{43}$$

The three terms in this expression can be Fourier-transformed individually. Their inverse Fourier transforms are, up to a singular part proportional to $\delta(\boldsymbol{r})$:

$$\frac{q_x^4}{q^4} \to \frac{-x^4 - 6x^2y^2 + 3y^4}{8\pi r^6}, \tag{44}$$

$$\frac{q_x^2 q_y^2}{q^4} \to \frac{-x^4 + 6x^2y^2 - y^4}{8\pi r^6}, \tag{45}$$

$$\frac{q_y^4}{q^4} \to \frac{3x^4 - 6x^2y^2 - y^4}{8\pi r^6}. \tag{46}$$

We thus get, in real space,

$$\Psi(x,y) = \frac{\alpha}{8\pi r^6}\left[(-3+2\beta+2\delta-\beta\delta)x^4 + 6x^2y^2 + (1-2\beta-2\delta)y^4\right]. \tag{47}$$

We can re-write this expression in polar coordinates as

$$\Psi(r,\theta) = \frac{\alpha}{8\pi r^2}\left[(-3+2\beta+2\delta-\beta\delta)\cos(\theta)^4 + 6\cos(\theta)^2\sin(\theta)^2 + (1-2\beta-2\delta)\sin(\theta)^4\right]. \tag{48}$$

First, we see that the kernel decays as $\Psi \sim 1/r^2$. Then, the direction $\theta_{\max}$ where this kernel is maximal for any fixed distance r is given by

$$\theta_{\max} = \arccos\left(\frac{\sqrt{1+\beta+\delta}}{2}\right) = \arccos\left(\sqrt{\frac{3+\sin(\phi)+2\delta}{8}}\right). \tag{49}$$

III. DAMAGE MODEL

The model is two-dimensional. It assumes plane stresses and solves the momentum and constitutive equations given by Eq. (4) and (5) of the main text, with the dependance of the elastic modulus on the level of damage given by Eq. (3). The MC failure criterion is implemented at the local scale (the scale of the model element). It is extended to tensile stresses (Fig. 1).

At each numerical time step, the local state of stress, $(\sigma_1,\ \sigma_2)$ in the principal stresses space, is compared to the critical stress set by the MC criterion. Where the stress is over-critical, the local level of damage, d, is incremented. This increment is chosen so that to project the local state of stress back onto the failure envelope, as indicated by the point $(\sigma_1',\ \sigma_2')$ on Fig. 1. As the deformation is assumed to remain constant during damage events, i.e., the first effect of damage is the initiation of a stress redistribution between neighbouring elements that modifies the local state of stress and not strains, this projection is made along the line passing through the origin, in the principal stresses space. The numerical time step is chosen sufficiently small so that damage propagation does not evolve out of equilibrium and conditions remain quasi-static in the simulations.

IV. NUMERICAL IMPLEMENTATION OF THE DAMAGE MODEL

The domain and boundary conditions for the simulations are described and represented in Fig. 1(a) of the main text. Finite elements and variational methods are used to solve the time-discretized problem on a Lagrangian grid within the C++ environment RHEOLEF [6]. As the cumulative deformation of the simulated specimen is small (0.01%), the position of the grid nodes is not updated in time. This means that the forcings and shape coefficients used for the spatial discretization are defined relative to the initial position of the grid nodes. This simplification does not impact the results

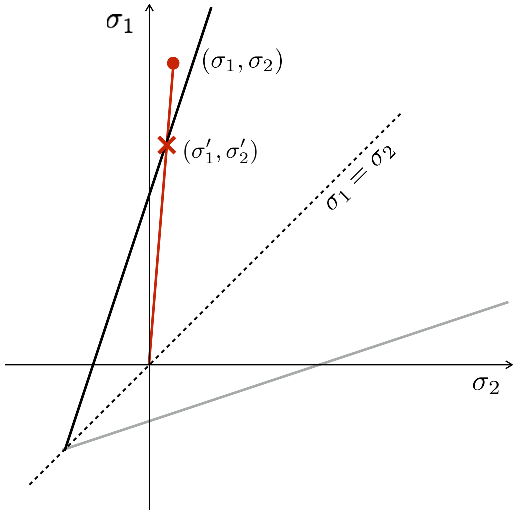

FIG. 1. MC damage criterion in the principal stresses plane (solid line). In the simulations performed here, the MC criterion is extended to tensile stresses and no truncation is used to close the envelope towards biaxial compression. The calculation of the distance to the damage criterion d_{crit}, defined by the intersection (σ_1', σ_2') of the line relating the state of stress (σ_1, σ_2) of a given element to the origin of the principal stress plane, is represented in red.

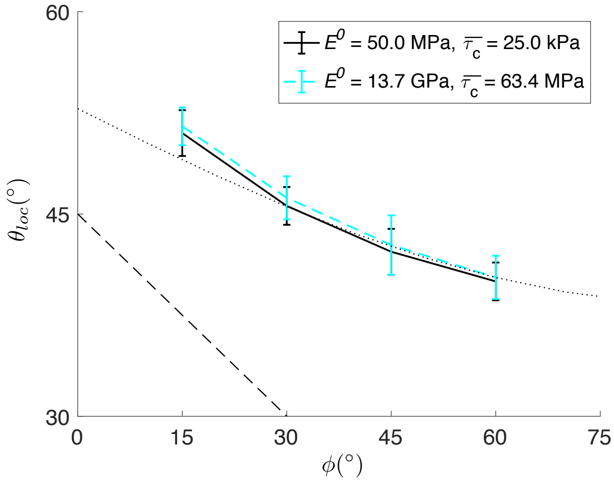

FIG. 2. Comparison of the mean localization angle, θ_{loc}, as a function of the internal friction angle, ϕ, in simulations using a minimal disorder and $E^0 = 50$ MPa and $\overline{\tau_c} = 25$ kPa, as in all model experiments presented in this paper (black solid curve), and $E^0 = 13.7$ GPa and $\overline{\tau_c} = 63.4$ MPa, as in the laboratory experiments on siltstone (core I) of [1] (cyan dashed curve). The error bars represent $\pm$ 1 standard deviation from the mean. In both cases, $\nu = 0.3$ and no confinement is applied.

reported here. Meshes with triangular elements are built using the Gmsh grid generator [7] and are chosen unstructured to avoid introducing preferential orientations in the damage localization. The average spatial resolution, Δx, is set by choosing the number N of elements along the short side of the domain, of length L, such that $\Delta x = L/(2N)$. In all simulations, N is set to 80 and the mesh grid counts 33858 elements.

The ratio of the undamaged elastic modulus, E^0, and of the mean (or median) value of cohesion, $\overline{\tau_c}$ (see main text), is the same in all simulations and is chosen to be representative of a natural quasi-brittle material (rock or ice). We have used $E^0 = 50\,\mathrm{MPa}$ and $\bar{\tau}_c = 25\,\mathrm{kPa}$ in our simulations. The specific values of these parameters do not affect our results with respect to the angle of localization, as long as they ensure that the simulated mechanical behavior is quasi-brittle (see Fig. 2).

Three mechanical parameters are varied in the simulations presented in the main text: (1) the local internal friction angle, ϕ, (2) Poisson's ratio, ν and (3) the confinement ratio, R. Additionally, the level of disorder introduced in the local critical strength of the material (i.e., the local value of the material's cohesion, τ_c) is varied via the proportion, a, of model elements for which τ_c is drawn randomly from a uniform distribution of values (referred to in the main text as the proportion of *inclusions*) and the width, η, of that uniform distribution (referred to as the *strength* of the disorder). The range of values for each parameter is summarized in Table II. For each set of parameters, an ensemble of 25 simulations is run to estimate the average orientation of the fault. All simulations are initialized with an undamaged material with uniform elastic modulus and stopped after the formation of a macroscopic fault and cessation of the damage activity (see Fig. 1(b) of main text).

We checked that neither the chosen model resolution nor the domain aspect ratio (1 or 2; square or rectangular domain) impacts the damage initialization, propagation and localization and the numerical experiments presented here. Figure 3(a) compares $\theta_{\mathrm{loc}}(\phi)$ for a square domain ($L \times L$, red lines) and rectangular domain ($L \times L/2$, black lines) in the case of minimal disorder (solid lines) and of a weak disorder ($\eta = 0.05$, $a = 1$, dashed-dotted lines). The case of minimal disorder are related parameters η and a is described in the main text. The results are equivalent in the limits of the calculated error bars (equivalent to 2 standard deviations of the mean θ_{loc}). The same is true when changing the model resolution between $N = 40, 80, 160$, which is represented on Fig. 3(b) also for the cases of minimal disorder (solid lines) and weak disorder ($\eta = 0.05$, $a = 1$, dashed-dotted lines).

V. DETERMINATION OF THE FAULT ORIENTATION

The orientation of the simulated localization pattern in the post-macro-rupture regime is estimated using a projection histogram method, similar to the Hough transform used to analyze the position and direction of linear structures in various types of imaging [e.g., 14, 15]. With

Parameters		Values
Internal friction angle	ϕ	$15°, 30°, 45°, 60°$
Poisson's ratio	ν	$0, 0.1, 0.2, 0.3, 0.4, 0.5$
Confinement ratio	R	$0\%, 10\%, 20\%$
Disorder - strength	η	0.05 ("weak") and 0.5 ("strong")
Disorder - proportion of inclusions	a	10^{-4}, 10^{-3}, 10^{-2}, 10^{-1}, 1

TABLE II. List of parameters varied in the simulations and their range of values.

this approach, the distribution histogram of a field value is calculated when projecting that field in a particular direction, β. By calculating projection histograms in all directions, the method allows detecting the principal orientations of linear features. Projection histograms of the field of damage are calculated as follow.

The instantaneous field of damage $d(\boldsymbol{r})$ simulated on an unstructured grid is first interpolated onto a structured square elements grid of similar size ($N \times 2N$) using a nearest neighbor interpolation. The origin of the rectangular image is defined as the lower left corner of coordinates $(x, y) = (0, 0)$ and the direction, β, is defined relative to the axis $y = 0$. Hence the position of the center of any grid element (x, y) can be written in polar coordinates as $(r\cos(\beta), r\sin(\beta))$, where $r = \sqrt{x^2 + y^2}$ (Fig. 4(a)).

Any given direction $0° \leq \beta \leq 180°$ defines a line D (Fig. 4(a), dashed white line) passing through the origin. For all positions r along that line, the average level of damage of the grid elements found along the line D' perpendicular to D is calculated (solid white line, Fig. 1a, main text). The result, denoted $\bar{d}_p(\beta, r)$, is the projection histogram in the direction β. The number of grid elements over which $\bar{d}_p(\beta, r)$ is calculated is not constant with r and is smaller near the corners of the domain. Hence a minimum number of points $N/4$ is imposed as a threshold for the calculation of $\bar{d}_p(\beta, r)$. We checked that (1) the resolution of the regular square grid onto which the simulated fields of damage are interpolated and (2) our choice of threshold for the minimum number of points for the calculation of $\bar{d}_p(\beta, r)$ have no effect on the results presented here.

The localization angle, $\theta_{\rm loc}$, is calculated using the absolute maximum value of the projection histogram for all values of β and r, as

$$\theta_{\rm loc} = \beta \ \text{ if } \beta < 90°, \tag{50}$$

$$= 180° - \beta \ \text{ if } \beta > 90°. \tag{51}$$

In the case of conjugate or multiple linear features, $\theta_{\rm loc}$ corresponds to the orientation of the *one* linear feature that returns the maximum in $\bar{d}_p$ (i.e., the most localized or most damaged feature).

[1] B. Haimson and J. W. Rudnicki, "The effect of the intermediate principal stress on fault formation and fault angle in siltstone," J. Struct. Geol. **32**, 1701 – 1711 (2010), fault Zones.

[2] E. M. Schulson, A. L. Fortt, D. Iliescu, and C. E. Renshaw, "On the role of frictional sliding in the compressive fracture of ice and granite: Terminal vs. post-terminal failure," Acta Mater. **54**, 3923 – 3932 (2006b).

[3] A. Haied, D. Kondo, and J. P. Henry, "Strain localization in Fontainebleau sandstone," Mech. Cohes.-Frict. Mater. **5**, 239–253 (2000).

[4] A. Hackston and E. Rutter, "The Mohr–Coulomb criterion for intact rock strength and friction – a re-evaluation and consideration of failure under polyaxial stresses," Solid Earth **7**, 493–508 (2016).

[5] J. P. Bardet, "A comprehensive review of strain localization in elastoplastic soils," Comput. Geotech. **10**, 163–188 (1990).

[6] Saramito2015, *Efficient C++ finite element computing with Rheolef* (CNRS-CCSD ed., 2015) http://cel.archives-ouvertes.fr/cel-00573970.

[7] C. Geuzaine and J.-F. Remacle, "Gmsh: A 3-d finite element mesh generator with built-in pre- and post-processing facilities," International Journal for Numerical Methods in Engineering **79**, 1309–1331 (2009).

[8] J. Kierfeld and V. M. Vinokur, "Slow crack propagation in heterogeneous materials," Phys. Rev. Lett. **96**, 175502 (2006).

[9] Jérémie Vasseur, Fabian B. Wadsworth, Yan Lavallée, Andrew F. Bell, Ian G. Main, and Donald B. Dingwell, "Heterogeneity: The key to failure forecasting," Scientific Reports **5**, 13259 EP – (2015).

[10] Carl E. Renshaw and Erland M. Schulson, "Universal behaviour in compressive failure of brittle materials," Nature **412**, 897 EP – (2001).

[11] D. Amitrano, "Brittle-ductile transition and associated seismicity: Experimental and numerical studies and relationship with the b value," J. Geophys. Res. **108** (2003), 10.1029/2001JB000680.

[12] D. Amitrano, J.-R. Grasso, and D. Hantz, "From diffuse to localised damage through elastic interaction," Geophys. Res. Lett. **26**, 2109–2112 (1999).

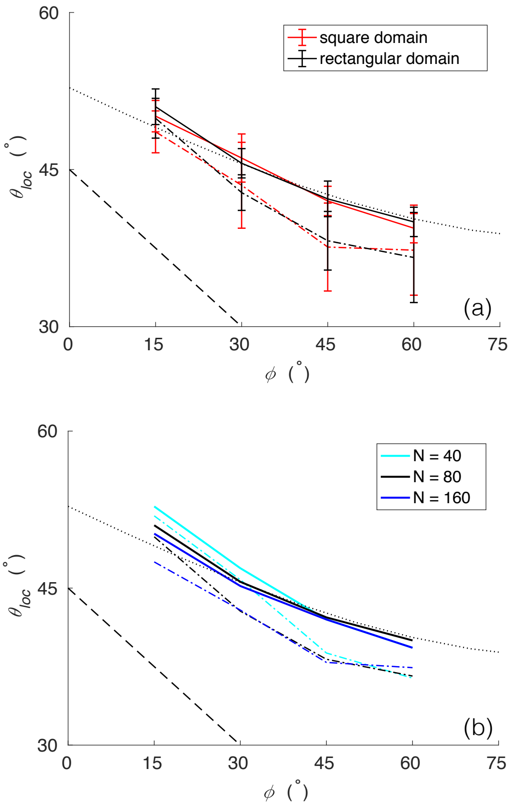

FIG. 3. (a) $\theta_{\mathrm{loc}}(\phi)$ for $\nu = 0.3$ and no confinement calculated for simulations using a square ($L \times L$) and a rectangular domain of aspect ratio 2 ($L \times L/2$) with the same number of mesh elements (160) along the long side of the domain (L). The solid lines shows the case of minimal disorder and the dashed-dotted lines, a case with $\eta = 0.05$ and $a = 1$. The error bars represent $\pm$ 1 standard deviation from the mean. (b) $\theta_{\mathrm{loc}}(\phi)$ for $\nu = 0.3$ and no confinement calculated for simulations using a rectangular domain of aspect ratio 2 ($L \times L/2$) with a number of mesh elements along the short side of the domain ($L/2$) of N = 40, 80 and 160. The solid lines shows the case of minimal disorder and the dashed-dotted lines, a case with $\eta = 0.05$ and $a = 1$. To improve the readability of the figure, the error bars have been omitted, but the standard deviation from the mean overall increases with decreasing resolution. On both panels the black dashed line shows θ_{MC} and the dotted line, θ_{LS} for $\nu = 0.3$ and no confinement.

[13] Stéphane Roux, Alex Hansen, Hans Herrmann, and Etienne Guyon, "Rupture of heterogeneous media in the limit of infinite disorder," Journal of Statistical Physics **52**, 237–244 (1988).

[14] Richard O. Duda and Peter E. Hart, "Use of the hough transformation to detect lines and curves in pictures," Commun. ACM **15**, 11–15 (1972).

[15] Roland Lehoucq, Jérôme Weiss, Bérengère Dubrulle, Axelle Amon, Antoine Le Bouil, Jérôme Crassous, and D Amitrano, "Analysis of image vs. position, scale and direction reveals pattern texture anisotropy," Frontiers in Physics **2**, 84 (2015).

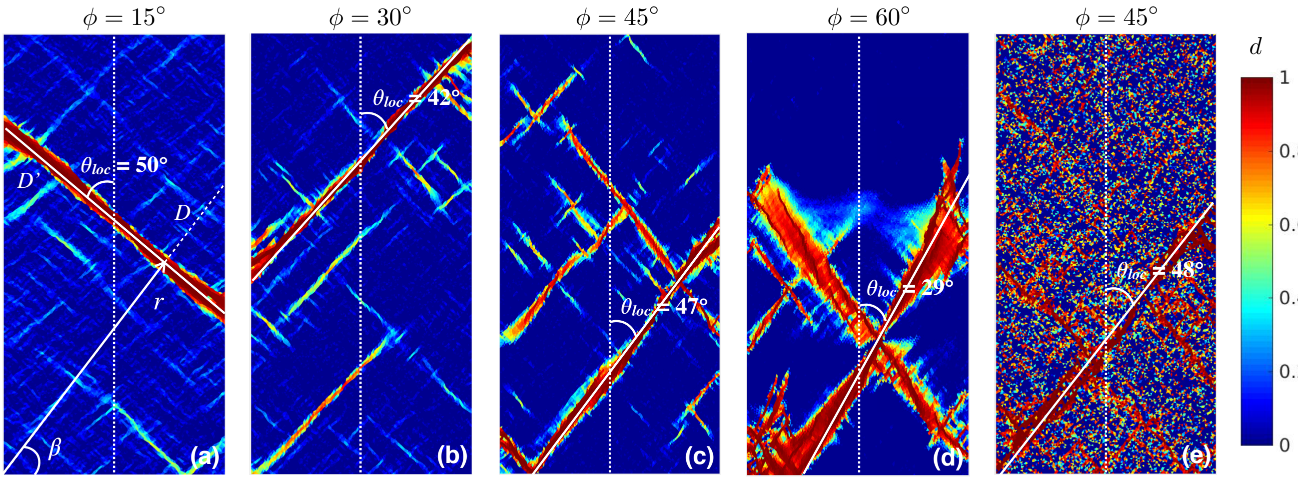

FIG. 4. Fields of the level of damage, d, simulated with $a = 1$, $\eta = 0.05$ and (a) $\phi = 15°$, (b) $\phi = 30°$, (c) $\phi = 45°$, (d) $\phi = 60°$. (e) Field of the level of damage simulated with $a = 1$, $\eta = 1$ and $\phi = 45°$. The white solid line indicates the fault and the value of localization angle, θ_{loc}, estimated by the projection histogram method is given in each case.